



A convolutional neural network model for SOH estimation of Li-ion batteries with physical interpretability

Gyumin Lee^{a,1}, Daeil Kwon^{b,1}, Changyong Lee^{c,*}

^a School of Business Administration, Ulsan National Institute of Science and Technology, Republic of Korea

^b Department of Industrial Engineering, Sungkyunkwan University, Republic of Korea

^c Department of Public Administration, Korea University, Republic of Korea



ARTICLE INFO

Communicated by: John E Mottershead

Keywords:

Li-ion battery
State-of-health estimation
Recurrence plot
Gramian angular field
Convolutional neural network

ABSTRACT

Previous machine learning models for state-of-health (SOH) estimation of Li-ion batteries have relied on prescribed statistical features. However, there is little theoretical understanding of the relationships between these features and SOH degradation patterns of the batteries. This study proposes a convolutional neural network model to estimate the future SOH value of Li-ion batteries in the early phases of qualification tests. First, capacity degradation data are transformed into two-dimensional images using recurrence plots and Gramian angular fields, highlighting the time-series features of the data. Second, five types of convolutional neural network models are developed to estimate the SOH values of Li-ion batteries for a certain cycle. Here, class activation maps are generated to present how the models arrive at their conclusions. Finally, the performance and reliability of the developed models are assessed under various experimental conditions. The proposed approach has the following two advantages: it automatically extracts important temporal features from the capacity degradation data for SOH estimation, and obtains the contribution of each temporal feature with respect to the estimation process. The experimental results on 379Li-ion batteries confirm that the proposed approach can reduce the time required for qualification tests to 50 cycles, under a 6% mean absolute percentage error.

1. Introduction

Li-ion batteries have been widely used across industries, from portable electronics and electric vehicles (EV) to power grids and energy-storage systems. Despite the COVID-19 impact, the market for Li-ion batteries is expected to grow at a compound annual growth rate of 12.3 % from 2021 to 2030 [1]. Regardless of their application, Li-ion batteries continuously degrade over the accumulation of charging and discharging cycles, even under regular usage [2]. There is a gradual decrease in battery capacity and gradual increase in internal impedance. The degradation rate is often affected by the operational and environmental conditions of Li-ion batteries, such as the charging and discharging rates, operating voltages and currents, and internal and environmental temperatures [3–7].

State-of-health (SOH) is a metric that quantifies the amount of battery degradation by measuring a battery's current capacity and impedance, compared with that of an unused (brand new) battery. Studies have presented different approaches for SOH estimation of

* Corresponding author.

E-mail address: changyonglee@korea.ac.kr (C. Lee).

¹ These authors contributed equally to this work.

Nomenclature

Forecast origin cycle The number of charging and discharging cycles to be used for estimating SOH values

Forecast target cycle The number of charging and discharging cycles for which future SOH values are estimated

Nomenclature for oversampling technique

a_{SMOTE} Randomly selected minority class sample

k_{SMOTE} Number of nearest neighbours of the minority class sample a_{SMOTE}

b_{SMOTE} Nearest neighbour samples of a_{SMOTE}

Nomenclature for time-series imaging method

x Time-series data

\vec{x} Trajectory vector extracted from time-series data

τ Time window

T Number of timestamps in the time-series data x

m Dimension

ϵ Epsilon; a prescribed threshold distance

$\theta(\cdot)$ Heaviside function

$\|\cdot\|$ Euclidean distance function

\tilde{x} Normalised time-series data

r Radius of data points in the polar coordinate system

ϕ Angle of data points in the polar coordinate system

t Timestamp; battery charging and discharging cycle

Nomenclature for convolutional neural network

$o(\cdot, \cdot)$ Output of convolution layer; feature map

$k(\cdot, \cdot)$ Weight of the kernel

$i(\cdot, \cdot)$ Input of convolution layer

m_o, m_k, m_i Row index of output, kernel, and input

n_o, n_k, n_i Column index of output, kernel, and input

$ReLU$ Rectified linear unit activation function

c Channel index

F^c Global average pooling

f_c Activation of channel c in the last convolution layer

O Final output value of CNN

w_c Weight of channel c

CAM Class activation map

Nomenclature for performance evaluation

MAE Mean absolute error

$MAPE$ Mean absolute percentage error

N Number of data samples

SOH_i^t Actual SOH value of the i th test sample at forecast target cycle t

\widehat{SOH}_i^t Estimated SOH value of the i th test sample at forecast target cycle t

Li-ion batteries exposed to operational and environmental stress conditions in the field. State-of-the-art approaches include electrochemical [8–10], equivalent circuit [11–13], and data-driven [14–28] modelling. Electrochemical modelling aims to capture all key behaviours of Li-ion batteries, with a large number of unknown parameters based on the understanding of electrochemical reactions between electrodes and electrolytes. Equivalent circuit modelling describes the dynamics of battery behaviours using lumped models with a simplified combination of resistors, inductors, and capacitors. These approaches require detailed battery specifications and demanding computational power to solve complex partial differential equations; thus, they may not be feasible for SOH estimation. Finally, data-driven modelling has emerged with continuous improvements in computational power and machine learning algorithms.

Recent data-driven approaches have focused on modelling the nonlinearity and heterogeneity of the capacity degradation trends of Li-ion batteries. They can be classified into the following two categories: classification and regression. Classification approaches identify the onset of the battery's anomalous SOH degradation in the early phases of charging and discharging cycles. For instance, Saxena et al. [22] presented a one-class support vector machine (SVM) to identify anomalous batteries. Lee et al. [14] calculated the radius of curvature of the nonlinear SOH degradation curve to detect the inflection points in charging and discharging cycles. Lee et al. [15] developed a capacity-fading behaviour analysis method to distinguish between unhealthy and healthy batteries based on local outlier factors, kernel density estimation, and a hidden Markov model. Regression approaches estimate the future SOH value of Li-ion batteries based on the temporal characteristics observed in the capacity degradation data. For instance, Kim et al. [16] proposed a

shifting kernel particle filter approach to accurately predict the remaining useful life (RUL) of Li-ion batteries, including those with heterogeneous degradation. Widodo et al. [23], using time-series features extracted by sample entropy algorithms, developed a prognostic framework for battery health based on an SVM and a relevance vector machine. Chaoui and Ibe-Ekeocha [24] proposed an autoregressive architecture based on recurrent neural networks (RNNs) for SOH and state-of-charge (SOC) estimation. Razavi-Far et al. [25] presented an integrated imputation prediction scheme to assess the RUL of Li-ion batteries with missing observations based on extreme learning machines. Ungurean et al. [26] presented a neural network architecture based on gated recurrent unit (GRU) for online prediction of battery health. Finally, Li et al. [27] suggested a prognostic framework to predict the SOH and RUL of Li-ion batteries using a variant of long short-term memory (LSTM) shared by multiple cells without mutual interference.

However, while machine learning models have been useful in identifying unhealthy batteries and estimating the SOH value of Li-ion batteries, the results of previous studies cannot be easily generalised and deployed in practice, due to various reasons. First, previous models relied on prescribed statistical features (e.g., changes and fluctuations in the SOH values over cycles), despite the lack of theoretical understanding of the relationships between these features and SOH degradation patterns of the batteries [15,28]. Note that, the important features may differ across the types of Li-ion batteries and operational and environmental conditions, even for a single type of Li-ion battery [14]. Hence, any proposed approach should be more effective in feature selection. Second, most previous studies have used capacity degradation data with a small sample size (less than 30), restricting the scope of analysis to certain experimental conditions for the SOH estimation [14–16,18–27]. Additional data samples should be used to diversify the scope of the analysis and enhance the richness of the potential implications. Finally, the studies have mainly relied on black-box models, whose internal mechanisms are not revealed. Given the use of black-box models, it is difficult for practitioners to fully understand the relationship between the temporal dynamics in capacity degradation behaviour of the Li-ion batteries and SOH estimation results. Therefore, black-box models should be extended to interpretable models to provide insight into methods that improve machine learning models and qualification testing procedures [29]. Study [17] partially addressed the above-mentioned issues by using a dataset consisting of 124 commercial LFP/graphite Li-ion battery cells with different ranges of cycle lives and adopting a regularised linear model that provides high interpretability. However, they relied on their domain knowledge to select the statistical features related to charging and discharging of batteries, and they interpreted the linear model based only on the prescribed range of cycles. This study extends [17] by using a convolutional neural network to extract important features from the capacity degradation data automatically and using a visual explanation method called class activation mapping to investigate the importance of temporal features over any range of cycles.

Considering these issues, we propose a convolutional neural network (CNN) model to estimate the future SOH value of Li-ion batteries in the early phases of qualification tests. When used for SOH estimation, the CNN model can automatically derive important features from the capacity degradation data. Moreover, it has a lower computational complexity and cost compared with previous RNN-like models, such as LSTM and gated recurrent unit (GRU). First, capacity degradation data is transformed into two-dimensional images using recurrence plots (RPs) and Gramian angular fields (GAFs), highlighting the nonstationary time-series features of the data. Second, five types of CNN models are developed to estimate the SOH values of Li-ion batteries for a certain cycle. Here, class activation maps are generated to present how the models arrive at their conclusions. Finally, the performance and reliability of the developed models are assessed under various experimental conditions. We applied the proposed approach to the capacity degradation data of 379Li-ion batteries, obtained from qualification tests. The analysis results confirmed that the proposed approach can reduce the time required for qualification tests to 50 cycles, which is less than two weeks in practice, under a 6 % mean absolute percentage error (MAPE). Moreover, the class activation maps demonstrated that the important temporal features (i.e., charging and discharging cycles) for estimating future SOH values, vary between healthy and unhealthy batteries. This logical interpretation of the estimation process shows that the developed CNN models can capture nonlinearity of the decrease in SOH values of the Li-ion batteries. This implication could also be identified by the symmetry-breaking in GAF images, which are physically interpretable.

The remainder of this paper is organised as follows: Section 2 explains the data and methodology used. Section 3 describes the experimental settings employed in this study. Section 4 presents the experimental results and discusses the performance and reliability of the proposed approach. Finally, Section 5 concludes the paper, states the limitations of this study, and suggests future research directions.

2. Data and methodology

2.1. Capacity degradation data

In this study, the capacity degradation data of 379 Li-ion batteries for EV, provided by a commercial automobile manufacturing company, are used as the initial dataset. The capacity degradation data are obtained from ongoing reliability tests during which Li-ion batteries are repeatedly charged and discharged, and the changes in their SOH are monitored simultaneously according to usage. The SOH is defined as the ratio of a battery's remaining capacity to its initial value, as formulated in Eq. (1). The batteries have the same nominal capacity at the beginning of the qualification tests, the SOH always starts from 1.0 as it represents the rate of change in the battery capacity.

$$SOH(t) = \frac{C(t)}{C(0)} \quad (1)$$

where $C(0)$ and $C(t)$ are the battery capacity values at the first cycle and cycle t in the qualification tests, respectively. The SOH values

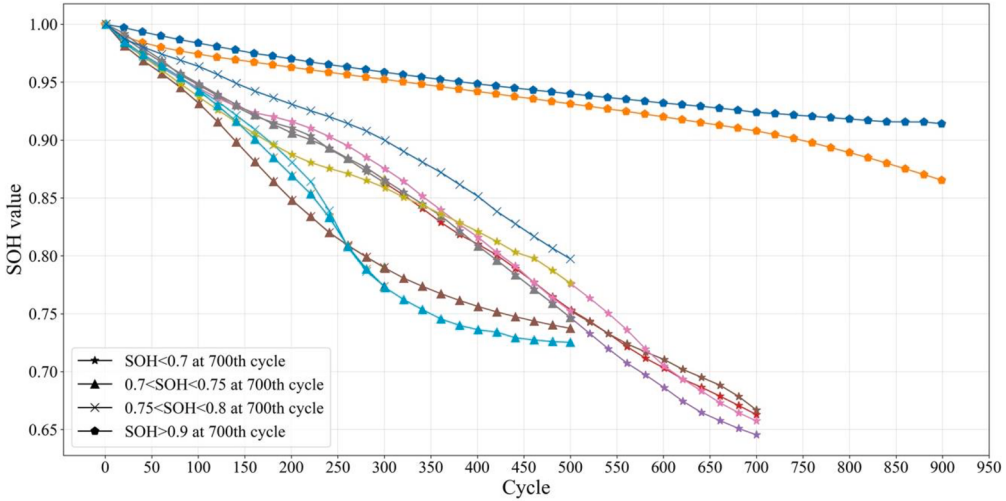


Fig. 1. A portion of capacity degradation data of Li-ion batteries.

were recorded at various lengths for each battery because the batteries reached their end of life (EOL) at different cycles. Generally, in the qualification tests on Li-ion batteries for EV, a battery is considered to have reached its EOL, if its SOH value drops below 0.7 at the 700th cycle. Accordingly, the SOH values of the batteries were measured till they reached their EOL or the 900th cycle, corresponding to approximately-three and a half months under accelerated stress conditions. In this context, the forecast target cycle is defined as the number of charging and discharging cycles for which the future SOH values are estimated (e.g., the 700th cycle), which could be used as a temporal criterion for judging a Li-ion battery's EOL.

Fig. 1 shows a portion of the initial dataset. Consistent with the results of previous studies, inflection points are observed between the 200th and 250th cycles [15]. A gradual SOH degradation is observed before the inflection point, regardless of the Li-ion battery's type (i.e., healthy and unhealthy batteries). The SOH degradation of unhealthy Li-ion batteries starts to accelerate at certain points between the 200th and 250th cycles. Moreover, every battery exhibits its own capacity degradation pattern, implying that nonlinear models are more appropriate than linear models for SOH estimation.

2.2. Methodology

2.2.1. Synthetic minority oversampling technique

In our initial dataset, the numbers of data samples available for SOH estimation differ according to the forecast target cycles, because the SOH values were recorded at various lengths for each battery sample. For instance, if a battery reaches its EOL in the 350th cycle, it cannot be used to train a machine learning model to predict the SOH value at the 700th cycle. Moreover, the SOH values for each forecast target cycle are imbalanced. For instance, most SOH values of the data samples range from 0.7 to 0.8 in the 700th cycle, whereas only a few samples show an SOH value greater than 0.9 in the 700th cycle.

We employ a synthetic minority oversampling technique (SMOTE) to complement the rarely observed SOH degradation patterns and avoid biased estimation towards specific SOH values. SMOTE, introduced by [30], generates new synthetic data samples through the linear interpolation of minority class samples. Specifically, this method first randomly selects a minority class sample a_{SMOTE} and finds its k_{SMOTE} th nearest minority class neighbours. The synthetic data sample is then generated as a convex combination of a_{SMOTE} and one of the randomly chosen k_{SMOTE} th nearest neighbours, b_{SMOTE} . Although SMOTE is useful in compensating for imbalanced data, it can be problematic to use it in practice because it often constructs a “bridge,” consisting of unrealistic synthetic data samples, between typical minority class samples and outliers. This is because SMOTE treats all minority class samples fairly, regardless of whether they are outliers or not. To overcome this drawback, Borderline SMOTE, which generates synthetic data samples using only the samples on the border of majority and minority classes, [31] has been suggested. Using the advantages of both oversampling methods, the proposed approach combines SMOTE and Borderline SMOTE to generate new data samples, considering both generality and specificity.

2.2.2. Recurrence plots and Gramian angular fields

The capacity degradation data employed in this study are a type of time-series data that can be characterised by time-dependent signal information and may not be appropriate as an input to the CNN models. Hence, we employ two major time-series imaging methods, namely, recurrence plots and Gramian angular fields, to transform the capacity degradation data into two-dimensional images, highlighting the time-series features of the data. These methods have been designed to represent univariate time-series data as a square matrix, considering temporal correlations within the data. Thus, they have been applied to CNN models that accept two-dimensional images as input. Several studies have reported that the use of time-series imaging methods with CNNs

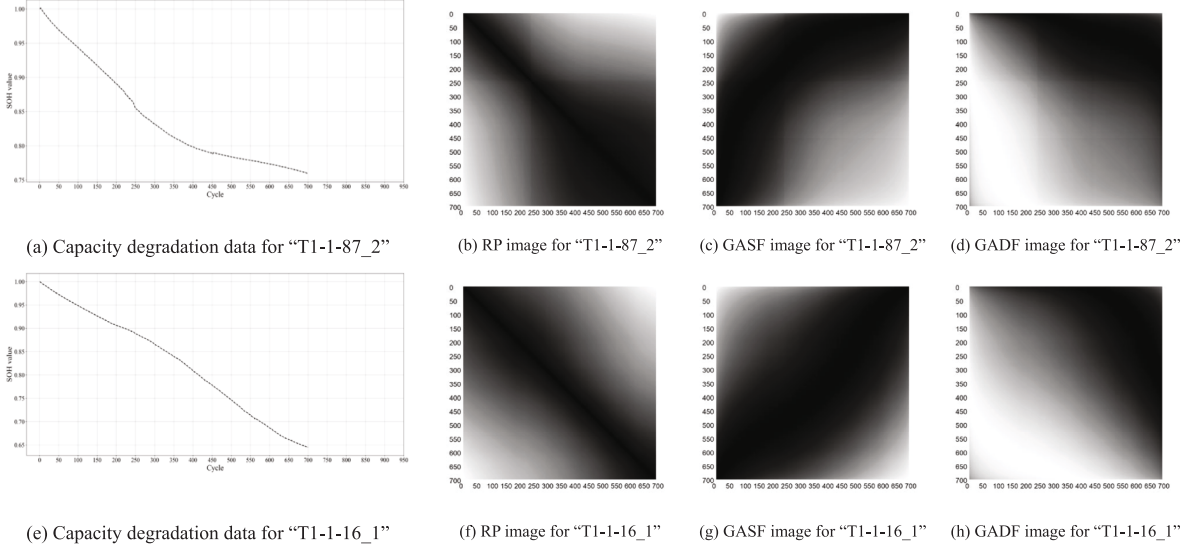


Fig. 2. Examples of the capacity degradation data and corresponding RP and GAF images.

demonstrates better performance in classification and regression tasks, compared with the use of raw time-series [32,33].

First, RP is a method for measuring the distance between trajectories, $\vec{x}_i = (x_i, x_{i+\tau}, \dots, x_{i+(m-1)\tau})$, $\forall i \in \{1, \dots, T-(m-1)\tau\}$, extracted from time-series data, $x = (x_1, x_2, \dots, x_T)$ [34]. This method reveals the points at which some trajectories return to a previous state, as formulated in Eq. (2).

$$R_{ij} = \theta(\epsilon - \|\vec{x}_i - \vec{x}_j\|), i, j = 1, \dots, T', \text{ where } T' = T - 1 \quad (2)$$

where T and T' are the number of timestamps in the time-series x and number of trajectories \vec{x} respectively, ϵ is a prescribed threshold distance, $\theta(\bullet)$ is the Heaviside function, and $\|\bullet\|$ is the Euclidean distance function. The resulting RP matrix involves *texture* and *typology* information of the time-series data, which are characteristic recurrent patterns exhibited at small and large scales, respectively. The *texture* of the time-series can be observed as follows: single dots that occur when the states are isolated due to their rarity, diagonal lines that occur if a trajectory parallels another trajectory, and vertical and horizontal lines that can occur when a state remains unchanged for a certain time window. The *typology* information provides a global impression of the time-series, categorised as follows: homogeneous RP for stationary systems, periodic RP for the systems with recurrent structures, drift RP for the systems with slowly varying parameters, and disrupted RP for the systems including extreme and rare events. Specifically, a two-dimensional phase space trajectory ($m = 2$) is generated from the capacity degradation data. Further, the RP matrix is calculated based on the distance between the states in the phase space. Here, we skip the thresholding step and directly generate the two-dimensional grey-level images.

Second, GAF encodes time-series data into two-dimensional images based on a polar coordinate system [32]. This method preserves the absolute temporal correlation because each point on the polar coordinate system is determined by its distance and angle from a reference point. GAF conversion consists of three steps. First, the time-series data, $x = (x_1, x_2, \dots, x_T)$, is normalised between 0 and 1, as shown in Eq. (3).

$$\tilde{x} = (\tilde{x}_1, \tilde{x}_2, \dots, \tilde{x}_T)$$

Where

$$\tilde{x}_i = \frac{x_i - \min(x)}{\max(x) - \min(x)} \quad (3)$$

Second, the time and amplitude corresponding to a point in the normalised time-series data, $\tilde{x} = (\tilde{x}_1, \tilde{x}_2, \dots, \tilde{x}_T)$, are converted to the radius and angle in the polar coordinate system, as defined in Eqs. (4) and (5), respectively.

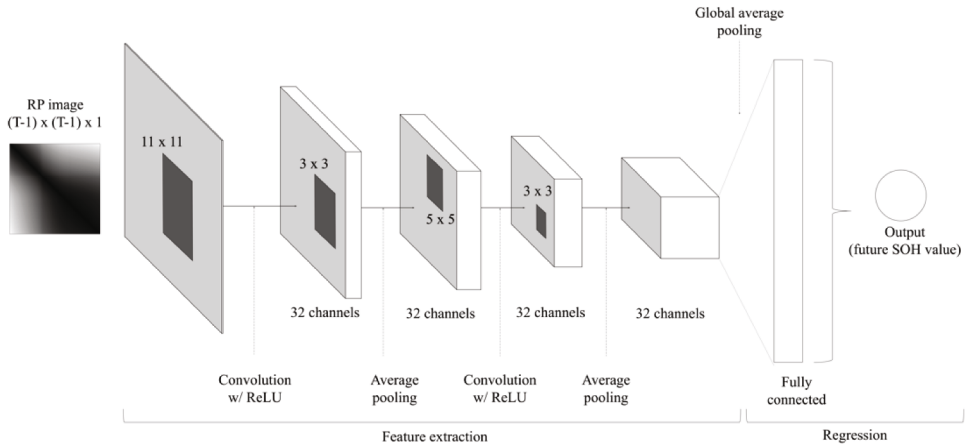
$$r = (r_1, r_2, \dots, r_T)$$

Where

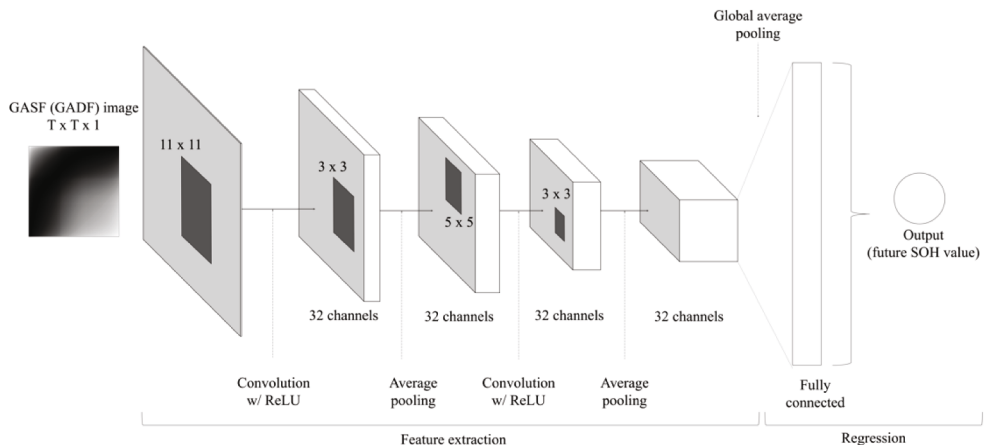
$$r_i = \frac{t_i}{T} \quad (4)$$

$$\phi = (\phi_1, \phi_2, \dots, \phi_T)$$

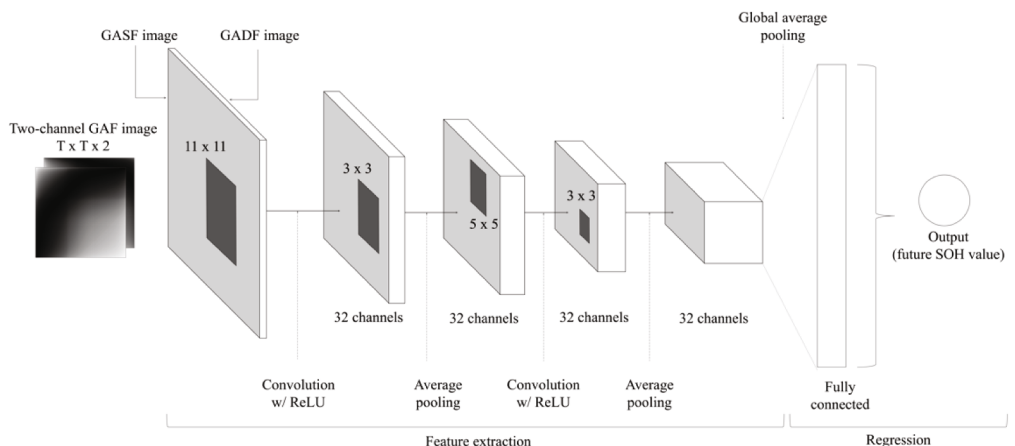
Where



(a) Architecture of the RP model

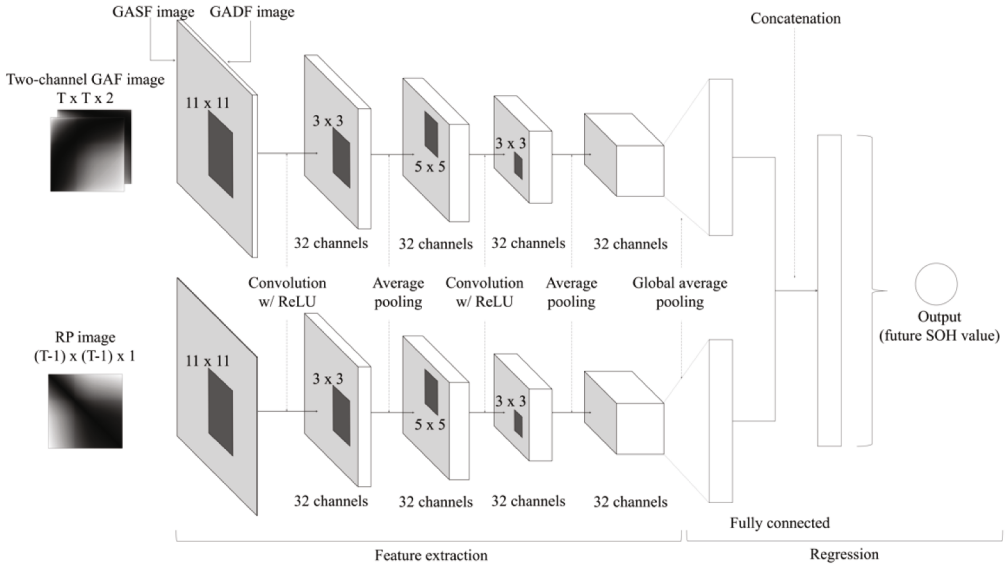


(b) Architecture of the GASF (GADF) model



(c) Architecture of the 2CH-GAF model

Fig. 3. The architecture of the five types of CNN models for SOH estimation.



(d) Architecture of the RP/2CH-GAF model

Fig. 3. (continued).

$$\phi_i = \arccos(\tilde{x}_i) \quad (5)$$

Finally, two forms of Gramian matrix, namely, the Gramian angular summation field (GASF) and Gramian angular difference field (GADF), are calculated, as shown in Eqs. (6) and (7), respectively.

$$GASF = \begin{bmatrix} \cos(\phi_1 + \phi_1) & \dots & \cos(\phi_1 + \phi_T) \\ \vdots & \ddots & \vdots \\ \cos(\phi_T + \phi_1) & \dots & \cos(\phi_T + \phi_T) \end{bmatrix} \quad (6)$$

$$GADF = \begin{bmatrix} \sin(\phi_1 - \phi_1) & \dots & \sin(\phi_1 - \phi_T) \\ \vdots & \ddots & \vdots \\ \sin(\phi_T - \phi_1) & \dots & \sin(\phi_T - \phi_T) \end{bmatrix} \quad (7)$$

Fig. 2 illustrates the capacity degradation data of the Li-ion battery samples and the corresponding RP, GASF, and GADF images. As mentioned, previously, the inflection point at which the decrease in the SOH value starts to accelerate, is often observed between the 200th and 250th cycles in the capacity degradation data. The transformed images represent the capacity degradation pattern while preserving the temporal information of the data. Particularly, the inflection point is observed in Fig. 2, as a distinct pattern at certain coordinates corresponding to the cycles between the 200th and 250th cycles. Although the global trend of the capacity degradation appears to be similar across Li-ion batteries, the transformed images can capture slight differences in the capacity degradation patterns based on the temporal correlations within the data. Hence, the RP and GAF imaging methods help produce appropriate input images for the CNN models, using the time-series capacity degradation data.

2.2.3. Convolutional neural network with the class activation map

A CNN is employed to assess the SOH values of Li-ion batteries in a certain cycle of interest in the early phases of the qualification tests. CNN is a class of deep learning models used to learn spatial hierarchies of features from grid pattern data such as images and texts [35]. When used for SOH estimation of Li-ion batteries, this method is more efficient than earlier approaches because it automatically extracts relevant features affecting the future SOH values of Li-ion batteries, from the two-dimensional images generated by the RP and GAF method. Moreover, it has fewer parameters than the RNN-like models.

Among the different architectures of CNN models, this study employs the CNN architecture with the class activation map proposed by Zhou et al. [36], to localise important regions in the input data used for prediction. Specifically, five types of models are developed based on the CNN architecture, depending on the time-series imaging methods for generating input images from the capacity degradation data, as shown in Fig. 3. The RP, GASF, and GADF models accept a single transformed image based on the RP, GASF, and GADF methods, respectively. The 2CH-GAF model accepts the two-channel GAF image, which comprises one channel for GASF image and another for GADF image. Finally, the RP/2CH-GAF model is designed to have two streams of feature extraction layers that parallelly accept the RP and two-channel GAF images. The shape of the input images is determined by the forecast origin cycle, which is the number of charging and discharging cycles to be used for estimating SOH values at the forecast target cycle. The RP and GAF

generate slightly different shapes of images because the number of trajectories for formulating RP matrix is $T - 1$, where T is the number of timestamps in a time-series. The RP image is in shape $(T - 1, T - 1)$, while the GAF image is in shape (T, T) . For instance, if the forecast origin cycle is set to 100, the shape of the input images will be $(99, 99)$ for RP, and $(100, 100)$ for GASF and GADF.

These five models share the base CNN architecture, which consists of two convolution layers, two average-pooling layers following each convolution layer, one global average pooling layer, and one fully connected layer. First, once the RP and GAF images representing the SOH degradation pattern are fed into the CNN model, the convolutional layer constructs feature maps using a convolutional operation that applies kernels. Specifically, the element-wise product between each element of the kernel and the input is calculated at each location of the input. Further, it is summed to produce the output value in the corresponding position of the feature map, as shown in Eq. (8).

$$o(m_o, n_o) = \sum_{m_k}^{M_k} \sum_{n_k}^{N_k} k(m_k, n_k) \bullet i(m_i + m_k, n_i + n_k), \quad m_o = 0, 1, \dots, M_o; n_o = 0, 1, \dots, N_o; m_k = 0, 1, \dots, M_k; n_k = 0, 1, \dots, N_k; m_i = 0, 1, \dots, M_i; n_i = 0, 1, \dots, N_i \quad (8)$$

In the equation, $o(\bullet, \bullet)$ is the value of the output, $k(\bullet, \bullet)$ is the weight of the kernel, $i(\bullet, \bullet)$ is the value of the input, and (M_o, N_o) , (M_k, N_k) and (M_i, N_i) indicate the sizes of the output, kernel, and input, respectively. The feature map is then passed through the rectified linear unit (ReLU) activation function, as shown in Eq. (9).

$$\text{ReLU}(x) = \max(0, x) \quad (9)$$

Second, the pooling layer reduces the dimensionality of the feature maps. Among the various pooling methods, we adopt an average-pooling method to select the mean value for each patch. Third, the global average pooling layer takes the average of all elements in each feature map at the last convolution layer while retaining the depth of the feature maps. Thus, global average pooling F^c results in a spatial average of the feature map for each channel, as shown in Eq. (10).

$$F^c = \sum_{x,y} f_c(x, y) \quad (10)$$

where $f_c(x, y)$ is the activation of channel c in the last convolution layer at spatial location (x, y) . Finally, the fully connected layer concatenates the feature maps as a one-dimensional vector, in which every input is connected to every output by a learnable weight. The activation function in the fully connected layer is an identity function. Thus, the final output value O is generated by the weighted sum of the values of the fully connected one-dimensional vector, as shown in Eq. (11).

$$O = \sum_c w_c \bullet F_c(x, y) \quad (11)$$

where w_c represents the weight of channel c corresponding to the final output value. Particularly, RP/2CH-GAF model has a parallel structure of two base CNN architectures that separately extract features from the RP and two-channel GAF images. An additional fully connected layer is placed to concatenate the two different one-dimensional vectors, representing the features separately extracted from the two types of images, as shown in Fig. 3(d).

The class activation maps are generated using the benefit of the global average pooling layer. By combining Eqs. (10) and (11), we obtain:

$$O = \sum_c w_c \sum_{x,y} f_c(x, y) = \sum_{x,y} \sum_c w_c \bullet f_c(x, y) \quad (12)$$

Further, from Eq. (12), we can observe that the higher w_c , the more the $f_c(x, y)$ affects the final output value. The class activation map CAM is defined as follows:

$$CAM(x, y) = \sum_c w_c \bullet f_c(x, y) \quad (13)$$

Accordingly, $CAM(x, y)$ directly indicates the importance of activation at spatial location (x, y) , leading to the final output value.

The development of the CNN model includes training and testing phases. In the training phase, we use a training dataset to learn the parameters and weights in the convolutional and fully connected layers to minimise the difference between the predicted and actual SOH values of the Li-ion batteries. Here, the gradient-based optimisation method (error backpropagation algorithm) is utilised to estimate the parameters of the model. For faster convergence, stochastic gradient descent (SGD) is used to update the parameters. Once trained, the model can predict the future SOH values of Li-ion batteries based on the SOH degradation patterns observed in the early phases of qualification tests.

2.2.4. Performance evaluation

A stratified fivefold cross-validation scheme is used to validate the proposed approach. Specifically, the dataset is partitioned into five folds, where four folds are used for training and the remaining fold is used as a test dataset in rotation. Given that our dataset is imbalanced, it is split in a stratified way such that each fold contains a similar distribution of SOH values at the forecast target cycle. This is attained by applying random sampling within each group, after the entire dataset is divided into multiple groups according to their SOH values at the forecast target cycle.

To evaluate the performance of the CNN models trained to forecast the SOH of Li-ion batteries, the MAE and MAPE are employed, as

Table 1
Experimental conditions.

Forecast origin cycles	50 100 150 200 250
Forecast target cycles	300 500 700

Table 2

Number of data samples employed in this study.

Forecast target	Number of data samples in the initial dataset	Number of data samples
		in the dataset after SMOTE
300	379	2,500
500	214	
700	111	

formulated in Eq. (14)-(15).

$$MAE = \frac{1}{N} \sum_{i=1}^N |SOH_i^t - \widehat{SOH}_i^t| \quad (14)$$

$$MAPE = \frac{1}{N} \sum_{i=1}^N \left(\frac{|SOH_i^t - \widehat{SOH}_i^t|}{SOH_i^t} * 100 \right) \quad (15)$$

where N is the number of test samples, and SOH_i^t and \widehat{SOH}_i^t are the actual and estimated SOH values of the i th test sample at forecast target cycle t , respectively. We use the MAE and MAPE for a fair evaluation of the performance, as MAE can directly demonstrate the differences between the actual and estimated SOH values, and MAPE can show a relative error. Consequently, the average perfold estimates are used to represent the performance of the proposed approach.

3. Experimental settings

Multiple experiments must be conducted in diverse contexts to examine the feasibility and practicality of the proposed approach. First, the cycle of interest for SOH estimation may differ across different Li-ion batteries. For instance, the Li-ion batteries for mobile phones are considered unhealthy if their SOH values drop below 0.8 during the 500th cycle, whereas those for automobiles are considered unhealthy if their SOH values drop below 0.7 during the 700th cycle. Moreover, the potential implications that can be derived by the proposed approach may differ according to the time when the approach is performed. In this respect, we consider five different forecast origin cycles (i.e., 50, 100, 150, 200, and 250), and three different forecast target cycles (i.e., 300, 500, and 700) for the experiments, as presented in Table 1. Particularly, the combinations of a forecast origin and target cycle, for which an experiment of the SOH estimation is conducted, are defined as forecast horizons. Second, SMOTE and Borderline SMOTE are applied to our initial dataset to resolve the data imbalance problem when training machine learning models for SOH estimation. Specifically, we divide the data samples in the initial dataset into five groups according to the SOH values at the forecast target cycle, as follows: [0,0.7), [0.7,0.75), [0.75,0.8), [0.8,0.85) and [0.85,1.0]. Synthetic data samples are generated for each subset to contain a total of 500 data samples including the data samples in the initial dataset; here, both SMOTE and Borderline SMOTE generate 250 new data samples each. Given the trade-off between the data imbalance problem and the data overfitting problem caused by an overabundance of synthetic data samples, we limit the number of data samples in each subset to 500, when the oversampling is performed. For each forecast target cycle, the resulting dataset contains 2,500 data samples to be used for model training. Table 2 presents the number of data samples in the initial dataset and the number of data samples when the synthetic samples are added using SMOTE and Borderline SMOTE.

4. Results

We applied the proposed approach to our dataset by varying the forecast origin and forecast target cycles for the chosen experimental conditions. Using MAE and MAPE as performance evaluation metrics, we examined the performance of the five CNN models trained for estimating SOH values, as reported in Table 3. The metric values marked in bold indicate the best performance for each forecast horizon. Overall, the performance evaluation metrics, especially the MAPE under 8 % (5 % on average) for every forecast

Table 3

Results of performance evaluation of CNN models.

(a) MAE results of the performance evaluation						
Forecast origin cycle	Forecast target cycle	CNN models		GADF	2CH-GAF	RP/2CH-GAF
		RP	GASF			
50	300	0.0560	0.0511	0.0528	0.0526	0.0517
	500	0.0462	0.0439	0.0469	0.0438	0.0433
	700	0.0496	0.0401	0.0469	0.0422	0.0411
100	300	0.0501	0.0484	0.0469	0.0414	0.0401
	500	0.0464	0.0446	0.0454	0.0443	0.0411
	700	0.0439	0.0375	0.0444	0.0385	0.0359
150	300	0.0467	0.0402	0.0433	0.0391	0.0341
	500	0.0423	0.0393	0.0389	0.0372	0.0356
	700	0.0318	0.0292	0.0279	0.0256	0.0248
200	300	0.0428	0.0378	0.0441	0.0377	0.0336
	500	0.0386	0.0345	0.0360	0.0344	0.0320
	700	0.0316	0.0259	0.0282	0.0249	0.0227
250	300	0.0385	0.0354	0.0396	0.0350	0.0302
	500	0.0370	0.0341	0.0355	0.0321	0.0300
	700	0.0293	0.0256	0.0280	0.0236	0.0211
(b) MAPE results of the performance evaluation						
Forecast origin cycle	Forecast target cycle	CNN models		GADF	2CH-GAF	RP/2CH-GAF
		RP	GASF			
50	300	7.54%	6.73%	7.00%	6.97%	6.83%
	500	6.09%	5.78%	6.19%	5.77%	5.71%
	700	6.55%	5.23%	6.14%	5.52%	5.37%
100	300	6.68%	6.46%	6.62%	5.55%	5.39%
	500	6.09%	5.89%	5.94%	5.85%	5.39%
	700	5.80%	4.93%	5.82%	5.03%	4.73%
150	300	6.29%	5.39%	5.86%	5.26%	4.63%
	500	5.59%	5.21%	5.14%	4.96%	4.74%
	700	4.22%	3.82%	3.65%	3.36%	3.24%
200	300	5.79%	5.07%	5.97%	5.03%	4.52%
	500	5.06%	4.57%	4.76%	4.55%	4.24%
	700	4.14%	3.39%	3.66%	3.24%	2.97%
250	300	5.16%	4.72%	5.23%	4.62%	3.96%
	500	4.84%	4.48%	4.69%	4.20%	3.93%
	700	3.87%	3.36%	3.66%	3.08%	2.74%

Table 4

Results of comparative study with other state-of-the-art approaches.

Forecast origin cycle	Forecast target cycle	Models			
		RP/2CH-GAF	ELM	GRU	LSTM
50	300	6.83 %	5.40 %	5.11 %	5.06 %
	500	5.71 %	7.18 %	8.09 %	7.56 %
	700	5.37 %	8.52 %	8.51 %	8.52 %
100	300	5.39 %	5.03 %	4.66 %	4.83 %
	500	5.39 %	6.39 %	5.91 %	6.92 %
	700	4.73 %	8.35 %	8.43 %	8.49 %
150	300	4.63 %	3.87 %	3.54 %	3.82 %
	500	4.74 %	5.35 %	4.20 %	5.22 %
	700	3.24 %	7.75 %	8.17 %	8.40 %
200	300	4.52 %	2.79 %	2.59 %	2.91 %
	500	4.24 %	4.60 %	4.61 %	4.58 %
	700	2.97 %	7.07 %	7.86 %	7.72 %
250	300	3.96 %	1.99 %	1.95 %	2.02 %
	500	3.93 %	4.17 %	4.29 %	4.33 %
	700	2.74 %	6.47 %	6.68 %	7.17 %

horizon, confirm that the proposed approach can predict future SOH values of Li-ion batteries using data from early phases of qualification tests. Moreover, MAE with an average of approximately 0.038, shows that the proposed approach can estimate actual SOH values with little deviation, given the range of the actual SOH values (i.e., [0,1]). Both performance evaluation metrics show a clear tendency according to the forecast horizons. In most cases, the larger the forecast origin cycle, the lower the estimation error. This is because, when the larger forecast origin cycle is set, the input images contain more information about the battery SOH degradation behaviour. Moreover, the larger the forecast target cycle, the higher the predictive performance. This is because the comprehensive

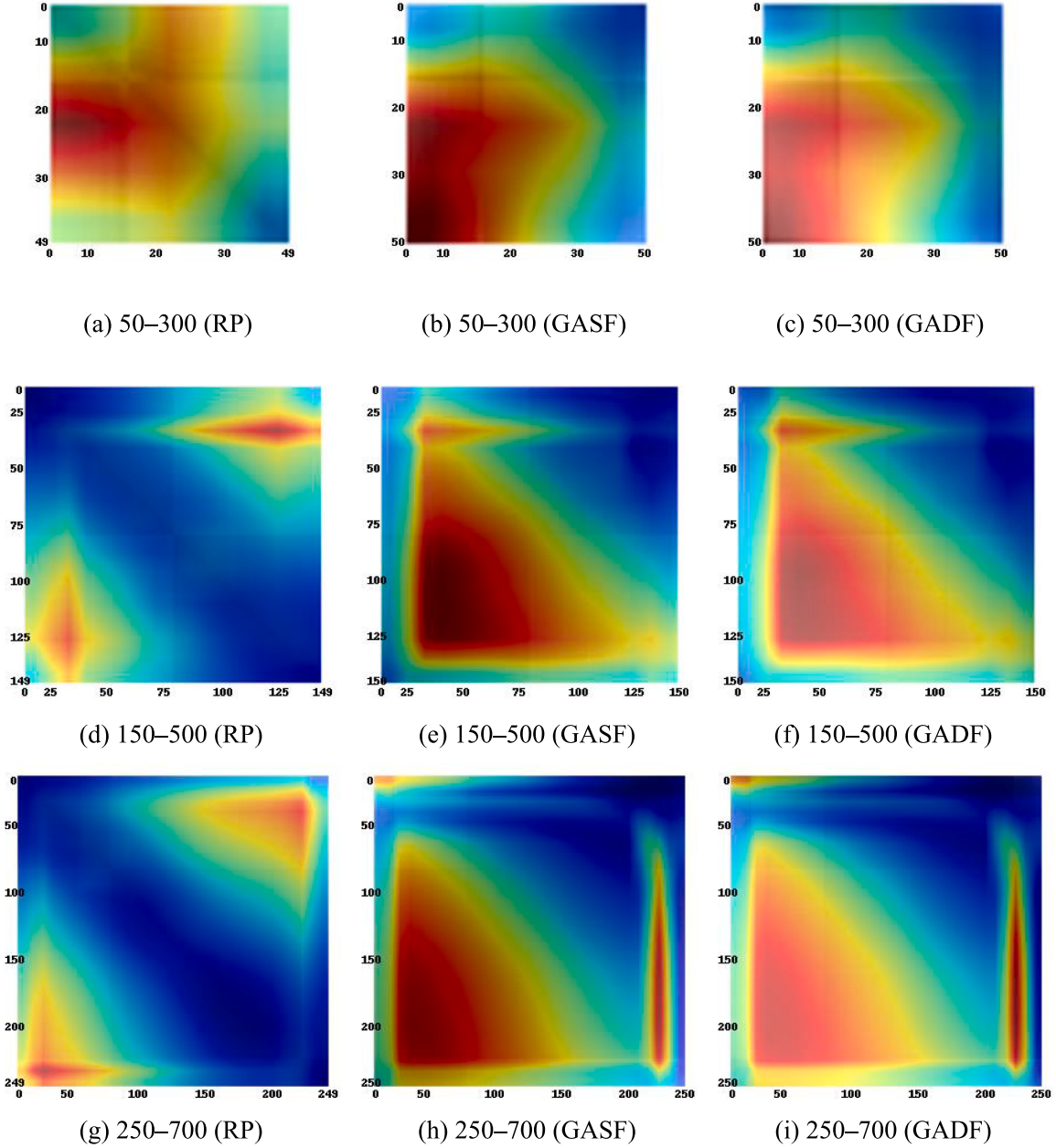


Fig. 4. Class activation maps for the battery sample “T1-1-13_1”.

correlation between SOH values in the early phases, represented by time-series imaging methods, indicates the long-term trends of battery SOH for longer forecast target cycles (e.g., the 700th cycle), where the healthy and unhealthy batteries are clearly differentiated. However, short-term estimation (e.g., the 300th cycle) can be influenced strongly by local trends surrounding the forecast target cycle, which hinders CNN models in estimating future SOH using the input images containing broad trends of SOH values.

In terms of model comparison, the RP/2CH-GAF model exhibited the highest predictive performance under most experimental conditions. This shows that the three different time-series imaging methods capturing different temporal characteristics of the SOH degradation data, produced a synergy effect in the SOH estimation. When the forecast origin cycle is set to 250 and the forecast target cycle is set to 700, the RP/2CH-GAF model achieved its best performance with an MAE of 0.0211 and MAPE of 2.74 %. In other words, the RP/2CH-GAF model near-perfectly estimated the future SOH values using the data collected from (approximately) two months of qualification tests under accelerated stress conditions. Therefore, considering the average predictive performance for various forecast

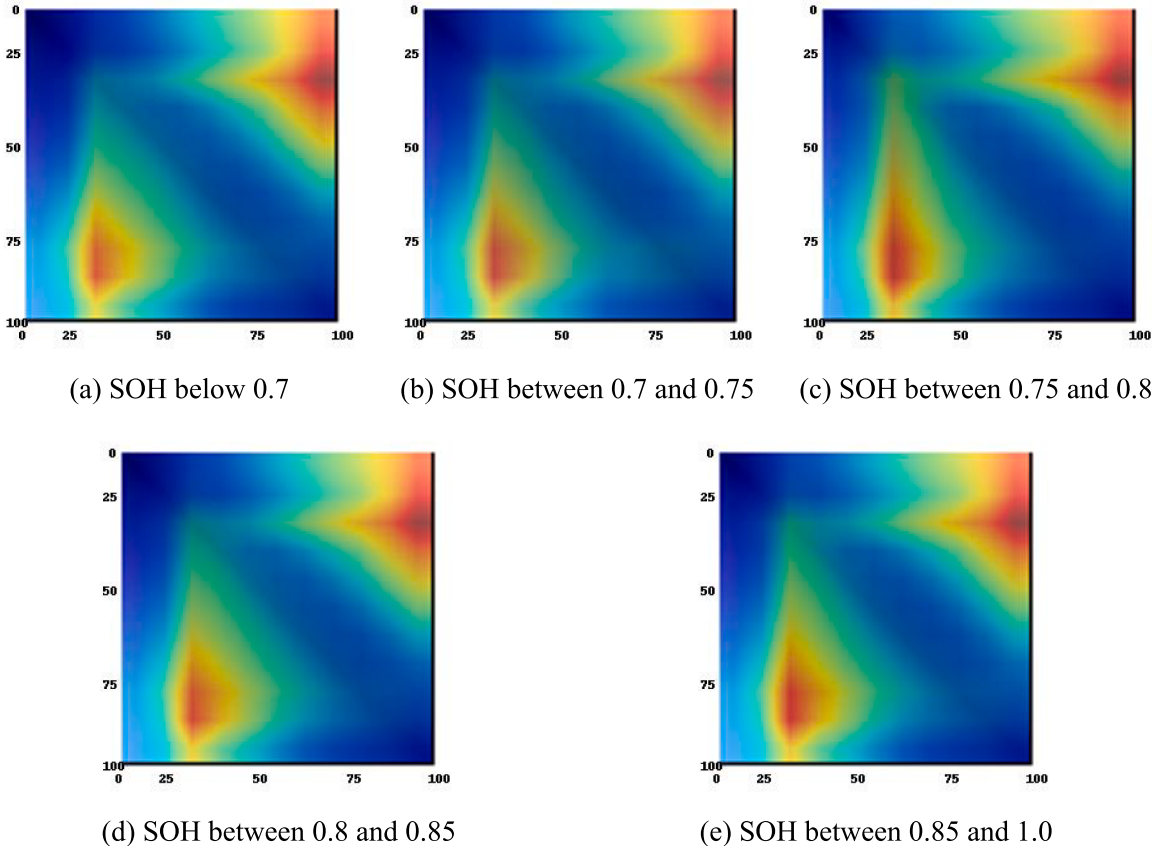


Fig. 5. The averaged class activation maps of the RP model according to the range of SOH values (forecast origin cycle = 100 and forecast target cycle = 700).

horizons, the RP/2CH-GAF model was identified as the best performing model. Regarding the CNN models accepting a single image as their input, the performance evaluation metrics were higher in the order of the GASF, GADF, and RP models. The results indicate that the Gramian angular field, considering the angular properties of time-series data, can represent more informative features of SOH degradation behaviour than the recurrence plots. In summary, these outcomes demonstrate that the proposed approach can be useful as a practical method for reducing the required time for qualification tests on Li-ion batteries.

An additional comparative study was conducted to compare the performance of the proposed approach to other state-of-the-art data-driven approaches for SOH estimation. Considering the employed dataset and analysis design of the proposed approach, we applied three neural network-based approaches, namely ELM [25], GRU [26], and LSTM [27], which aim to estimate the future SOH of Li-ion batteries using the observed SOH only. Table 4 presents the results of the comparative study where MAPE is used as the performance evaluation metric. The RP/2CH-GAF model showed the lowest performance when the forecast target cycle was set to 300. The presence of inflection points can cause a larger fluctuation in the SOH values around the 300th cycle. Thus, it becomes difficult to estimate SOH values using the RP and GAF images that capture global trends of SOH values during the forecast origin cycles. However, the RP/2CH-GAF model outperformed other models when the forecast target cycle was set to 500 or 700. Furthermore, the larger the forecast target cycle, the higher the predictive performance of the proposed approach, and lower the performance of the other approaches. This may be because the RP/2CH-GAF model considers the interrelationships among all changes in SOH values contained in the input images, whereas ELM, GRU, and LSTM emphasise the local trends of SOH values around the forecast target cycle. Therefore, we can conclude that the proposed approach is more useful and reliable than the previous approaches, especially for the SOH estimation of Li-ion batteries in practice, where early detection of unhealthy batteries is of utmost importance.

The analysis results imply the inconsistency of proportional decrease in SOH values over the entire life cycles can be effectively characterised and captured by the RP/2CH-GAF models. The two time-series imaging methods employed in this study can produce two-dimensional images from the SOH degradation data, which effectively represent the temporal dynamics within the data while preserving temporal dependency according to the cycles. Specifically, RP matrix involves the characteristic recurrent patterns exhibited by the change in the SOH values corresponding to the row and column indices, and two forms of Gramian matrix, GASF and GADF, represent the summation and difference between the SOH values corresponding to the row and column indices. When a battery is healthy, a proportional decrease in the SOH value produces a symmetrical shape across all types of images, especially along the

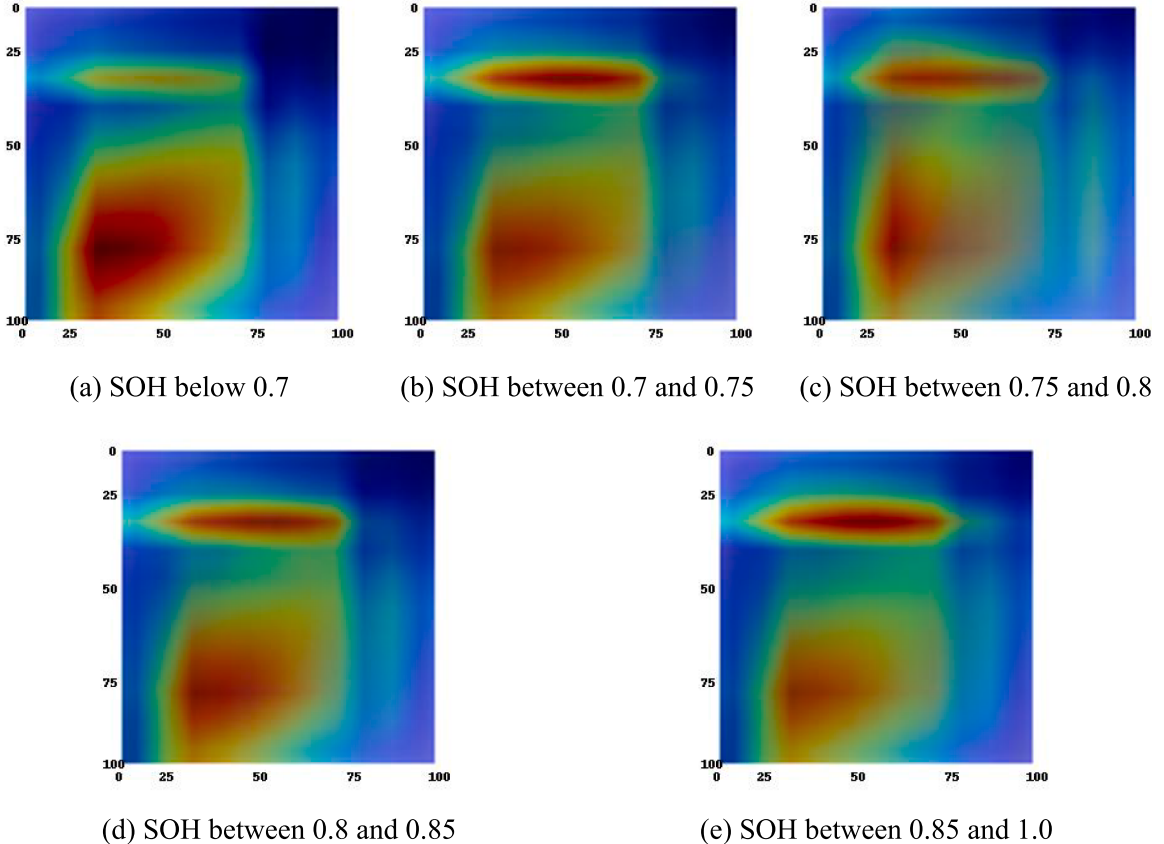


Fig. 6. The averaged class activation maps of the GASF model according to the range of SOH values (forecast origin cycle = 100 and forecast target cycle = 700).

diagonal line for RP and GASF and antidiagonal line for GADF. When a battery is unhealthy, a decrease in the SOH values is not proportional, indicating the presence of an inflection point. This results in symmetry-breaking across the RP, GASF, and GADF images, as shown in Fig. 2. These characteristics of the images offer physical interpretability of SOH values over the life cycles, allowing for general applicability to the unseen “out-of-distribution” cases that are not included in the training data but may be encountered in real-world system operations.

Further, we extracted the class activation maps for the best performing model (i.e., RP/2CH-GAF) to understand how the model arrived at its conclusions and examine how the logical interpretations about such estimation process are related to the physical interpretations provided by RP, GASF, and GADF images. Fig. 4 presents the class activation maps extracted from an unhealthy battery sample for various forecast horizons. Figs. 5-7 present the averaged class activation maps for the RP, GASF, and GADF images, constructed using the SOH degradation data during 100 cycles for each subset, grouped by SOH values at the 700th cycle (i.e., [0,0.7), [0.7,0.75), [0.75,0.8), [0.8,0.85), and [0.85,1.0]). Fig. 4 and Figs. 5-7 were obtained to investigate the local and global effects of the spatial locations in the input images (i.e., temporal features) on the SOH estimation, respectively. Specifically, Figs. 5-7 include the class activation maps extracted for a fixed forecast horizon (i.e., the 100th cycle as the forecast origin cycle and the 700th cycle as the forecast target cycle) to compare the model interpretations for the three time-series imaging methods. In the figures, the row and column indices indicate timestamps of the original time-series data for the input image. The blue and red regions represent the spatial locations in the input images that are “not activated” and “highly activated,” respectively.

Fig. 4 shows the class activation maps obtained from an unhealthy battery sample (i.e., its SOH value was under 0.7 at the 700th cycle) named “T1-1-13_1” for various forecast horizons. These maps exhibit the temporal features that highly contribute to SOH estimation when using the RP/2CH-GAF model, according to the forecast origin and target cycles. Particularly, Fig. 4(a)-(c), Fig. 4(d)-(f), and Fig. 4(g)-(i) present the class activation maps for the forecast horizons 50–300, 150–500, and 250–700, respectively. For the RP images in Fig. 4(a) and (d), there exist distinct symmetrically activated regions at both extreme ends of the antidiagonal line. These regions indicate the temporal correlation of the changes in SOH values between the early and later phases of qualification tests, showing that the rapid degradation of SOH during the corresponding period highly affects the model’s estimation process. In Fig. 4(a), which represents the class activation map for 50–300, almost all regions were activated, indicating that the changes in SOH values in most cycles equally contribute to the models’ estimation of the SOH values at the relatively early forecast target cycle (i.e., the 300th

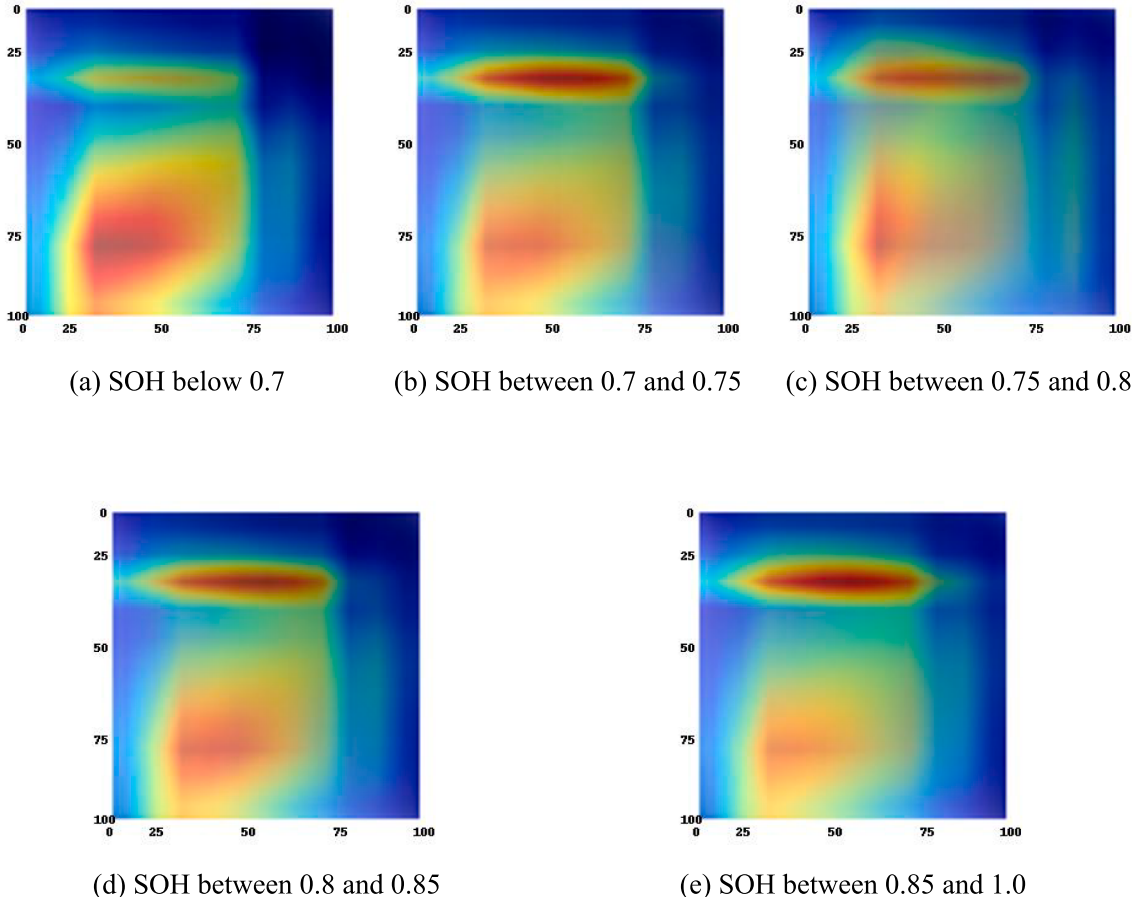


Fig. 7. The averaged class activation maps of the GADF model according to the range of SOH values (forecast origin cycle = 100 and forecast target cycle = 700).

cycle). The class activation maps for the GASF and GADF images were mostly identical because the regions in the left-half of the diagonal line were mainly activated for all forecast horizons, except that the maps for GADF were slightly brighter. A stick-shaped region at the rightmost of the class activation maps for 250–700, represents that the temporal correlations of the change in SOH values between the 250th and other cycles significantly contribute to the SOH estimation process. This confirms that the model considers the inflection point, which is usually observed between the 200th and 250th cycles, important for estimating the future SOH values. For more detailed results of model interpretation, the class activation maps of other representative battery samples for various forecast horizons are provided in Appendix.

In Fig. 5, the five averaged class activation maps for the RP images have similar activated regions located in both extreme ends of the antidiagonal line, for all ranges of SOH values at the 700th cycle. This indicates that the correlation of the changes in SOH values between early (about the 25th cycle) and later cycles (about the 75th cycle) in the qualification tests, strongly influences the model's decision-making for SOH estimation. The averaged class activation map for the SOH between 0.85 and 1.0 (Fig. 5(e)) was slightly more activated than that for the SOH below 0.7 (Fig. 5(a)). This demonstrates that, for the RP images, the changes in SOH values in the early phases of qualification tests contribute to the estimation process of the model more when a battery is healthy than when a battery is unhealthy. As mentioned, previously, in Figs. 6–7, the averaged class activation maps extracted for the two forms of Gramian angular field image were in similar shape, except that the ones for GADF were brighter. The class activation maps in Figs. 6–7 have similar activated regions; the horizontal line located near the 25th cycle, and the rectangle-shaped region that covers between the 50th and 100th cycles in rows and between the 25th and 75th cycles in columns. Additionally, the horizontal line was more activated when a battery was healthy, while the rectangle-shaped region was more activated when a battery was unhealthy. This shows that, for the GASF and GADF images, the changes in SOH values in the beginning are informative for predicting future SOH of healthy batteries, and the changes in SOH values during mid-early phases are useful for the model to estimate future SOH of unhealthy batteries. The results of class activation maps confirm that the logical interpretation of the models' estimation process and the physical interpretation using the transformed images of time-series data result in similar outcomes. Therefore, the proposed approach using CNN models with three time-series imaging methods can serve as a practical tool to support decision-making process of developing Li-ion batteries.

5. Conclusion

This study proposed a CNN approach using recurrence plots and Gramian angular fields as time-series imaging methods, to estimate future SOH values of Li-ion batteries in the early phases of qualification tests. To understand the SOH estimation process and verify the reliability of the models, this study employed class activation maps that present how the models arrive at their conclusions. The distinct feature of the proposed approach, compared with previous machine learning models, lies in its ability to automatically extract important temporal features from the capacity degradation data for SOH estimation. It can also obtain the contribution of each temporal feature with respect to the estimation process. The analysis results confirmed that the proposed approach can reduce the time required for qualification tests to 50 cycles, that is, less than a month in practice, under a 6 % mean absolute percentage error. Moreover, the class activation maps demonstrated that the important temporal features for estimating the future SOH values, varied between healthy and unhealthy batteries. This logical interpretation of the estimation process shows that the developed CNN models can capture nonlinearity of the decrease in SOH values of Li-ion batteries.

Despite these contributions, the limitations of this study suggest that our findings should be viewed cautiously. First, although many other factors affect the SOH values of Li-ion batteries, the proposed approach solely relies on the capacity degradation data. In this respect, the proposed approach can be further elaborated using other types of features, such as temperature and internal resistance. Second, the performance of the proposed approach may depend on the type of input images. In this respect, the performance of other time-series imaging methods that highlight capacity degradation behaviours, such as Markov transition fields [32,37], should be examined. Finally, the results and implications that can be derived by the proposed approach cannot be generalised easily because our case study is limited to one type of Li-ion batteries for automobiles. Moreover, the capacity degradation data employed in this study were generated through experiments which controlled various factors, such as temperature. Further testing on a wide range of Li-ion batteries under diverse experimental conditions is required to establish the external validity of our approach.

Declaration of Competing Interest

The authors declare that they have no known competing financial interests or personal relationships that could have appeared to influence the work reported in this paper.

Data availability

The data that has been used is confidential.

Acknowledgements

This work was supported by the National Research Foundation of Korea (NRF) grant funded by the Korean government (MSIT) (NRF-2020R1A4A4079904) and the National Research Foundation of Korea grant funded by the Korean government (MSIT) (NRF-2020R1F1A1066472).

References

- [1] Market Research Report, Lithium-Ion Battery Market with COVID-19 Impact Analysis, by Type (Li-NMC, LFP, LCO, LTO, LMO, NCA), Capacity, Voltage, Industry (Consumer Electronics, Automotive, Power, Industrial), & Region (North America, Europe, APAC & RoW) - Global Forecast to 2030, (2021). <https://www.marketsandmarkets.com/Market-Reports/lithium-ion-battery-market-49714593.html> (accessed December 6, 2021).
- [2] X. Hu, C.M. Martinez, Y. Yang, Charging, power management, and battery degradation mitigation in plug-in hybrid electric vehicles: A unified cost-optimal approach, *Mech. Syst. Signal Process.* 87 (2017) 4–16, <https://doi.org/10.1016/j.ymssp.2016.03.004>.
- [3] C.P. Yang, Y.X. Yin, S.F. Zhang, N.W. Li, Y.G. Guo, Accommodating lithium into 3D current collectors with a submicron skeleton towards long-life lithium metal anodes, *Nat. Commun.* 6 (2015) 8058, <https://doi.org/10.1038/ncomms9058>.
- [4] M. Li, J. Lu, Z. Chen, K. Amine, 30 Years of lithium-ion batteries, *Adv. Mater.* 30 (2018) 1–24, <https://doi.org/10.1002/adma.201800561>.
- [5] L. Zhang, W. Fan, Z. Wang, W. Li, D.U. Sauer, Battery heating for lithium-ion batteries based on multi-stage alternative currents, *J. Energy Storage.* 32 (2020), 101885, <https://doi.org/10.1016/j.est.2020.101885>.
- [6] Q. Wang, Z. Wang, L. Zhang, P. Liu, Z. Zhang, A novel consistency evaluation method for series-connected battery systems based on real-world operation data, *IEEE Trans. Transp. Electrif.* 7 (2021) 437–451, <https://doi.org/10.1109/TTE.2020.3018143>.
- [7] S. Saxena, Y. Xing, D. Kwon, M. Pecht, Accelerated degradation model for C-rate loading of lithium-ion batteries, *Int. J. Electr. Power Energy Syst.* 107 (2019) 438–445, <https://doi.org/10.1016/j.ijepes.2018.12.016>.
- [8] G. Jiang, L. Zhuang, Q. Hu, Z. Liu, J. Huang, An investigation of heat transfer and capacity fade in a prismatic Li-ion battery based on an electrochemical-thermal coupling model, *Appl. Therm. Eng.* 171 (2020), 115080, <https://doi.org/10.1016/j.applthermaleng.2020.115080>.
- [9] M. Daigle, C.S. Kulkarni, Electrochemistry-based battery modeling for prognostics, *PHM 2013 - Proc. Annu. Conf. Progn. Heal. Manag. Soc.* 2013. 5 (2013) 249–261. <https://doi.org/10.36001/phmconf.2013.v5i1.2252>.
- [10] J. Kim, H. Chun, M. Kim, S. Han, J.W. Lee, T.K. Lee, Effective and practical parameters of electrochemical Li-ion battery models for degradation diagnosis, *J. Energy Storage.* 42 (2021), 103077, <https://doi.org/10.1016/j.est.2021.103077>.
- [11] T. Feng, L. Yang, X. Zhao, H. Zhang, J. Qiang, Online identification of lithium-ion battery parameters based on an improved equivalent-circuit model and its implementation on battery state-of-power prediction, *J. Power Sources.* 281 (2015) 192–203, <https://doi.org/10.1016/j.jpowsour.2015.01.154>.
- [12] J. Sihvo, T. Roinila, D.I. Stroe, Novel fitting algorithm for parametrization of equivalent circuit model of Li-ion battery from broadband impedance measurements, *IEEE Trans. Ind. Electron.* 68 (2021) 4916–4926, <https://doi.org/10.1109/TIE.2020.2988235>.
- [13] X. Hua, C. Zhang, G. Offer, Finding a better fit for lithium ion batteries: A simple, novel, load dependent, modified equivalent circuit model and parameterization method, *J. Power Sources.* 484 (2021), 229117, <https://doi.org/10.1016/j.jpowsour.2020.229117>.
- [14] J. Lee, D. Kwon, M.G. Pecht, Reduction of Li-ion battery qualification time based on prognostics and health management, *IEEE Trans. Ind. Electron.* 66 (2019) 7310–7315, <https://doi.org/10.1109/TIE.2018.2880701>.

- [15] C. Lee, S. Jo, D. Kwon, M.G. Pecht, Capacity-fading behavior analysis for early detection of unhealthy Li-Ion batteries, *IEEE Trans. Ind. Electron.* 68 (2021) 2659–2666, <https://doi.org/10.1109/tie.2020.2972468>.
- [16] S. Kim, H.J. Park, J.-H. Choi, D. Kwon, A novel prognostics approach using shifting kernel particle filter of Li-ion batteries under state changes, *IEEE Trans. Ind. Electron.* 68 (4) (2021) 3485–3493.
- [17] K.A. Severson, P.M. Attia, N. Jin, N. Perkins, B. Jiang, Z. Yang, M.H. Chen, M. Aykol, P.K. Herring, D. Fragedakis, M.Z. Bazant, S.J. Harris, W.C. Chueh, R. D. Braatz, Data-driven prediction of battery cycle life before capacity degradation, *Nat. Energy.* 4 (2019) 383–391, <https://doi.org/10.1038/s41560-019-0356-8>.
- [18] X. Hu, J. Jiang, D. Cao, B. Egardt, Battery health prognosis for electric vehicles using sample entropy and sparse Bayesian predictive modeling, *IEEE Trans. Ind. Electron.* 63 (2015) 1–10.1109/TIE.2015.2461523.
- [19] D.E. Acuña, M.E. Orchard, Particle-filtering-based failure prognosis via sigma-points: Application to lithium-ion battery state-of-charge monitoring, *Mech. Syst. Signal Process.* 85 (2017) 827–848, <https://doi.org/10.1016/j.ymssp.2016.08.029>.
- [20] S. Kim, N.H. Kim, J.H. Choi, Prediction of remaining useful life by data augmentation technique based on dynamic time warping, *Mech. Syst. Signal Process.* 136 (2020), <https://doi.org/10.1016/j.ymssp.2019.106486>.
- [21] D. Wang, Y. Zhao, F. Yang, K.L. Tsui, Nonlinear-drifted Brownian motion with multiple hidden states for remaining useful life prediction of rechargeable batteries, *Mech. Syst. Signal Process.* 93 (2017) 531–544, <https://doi.org/10.1016/j.ymssp.2017.02.027>.
- [22] S. Saxena, M. Kang, Y. Xing, M. Pecht, Anomaly detection during lithium-ion battery qualification testing, 2018 IEEE Int. Conf. Progn. Heal. Manag. ICPHM 2018 (2018) 1–6, <https://doi.org/10.1109/ICPHM.2018.8448735>.
- [23] A. Widodo, M.C. Shim, W. Caesarendra, B.S. Yang, Intelligent prognostics for battery health monitoring based on sample entropy, *Expert Syst. Appl.* 38 (2011) 11763–11769, <https://doi.org/10.1016/j.eswa.2011.03.063>.
- [24] H. Chaoqui, C.C. Ibe-Ekeocha, State of charge and state of health estimation for lithium batteries using recurrent neural networks, *IEEE Trans. Veh. Technol.* 66 (2017) 8773–8783, <https://doi.org/10.1109/TVT.2017.2715333>.
- [25] R. Razavi-Far, S. Chakrabarti, M. Saif, E. Zio, An integrated imputation-prediction scheme for prognostics of battery data with missing observations, *Expert Syst. Appl.* 115 (2019) 709–723, <https://doi.org/10.1016/j.eswa.2018.08.033>.
- [26] L. Ungureanu, M.V. Micea, G. Carstoiu, Online state of health prediction method for lithium-ion batteries, based on gated recurrent unit neural networks, *Int. J. Energy Res.* 44 (2020) 6767–6777.
- [27] P. Li, Z. Zhang, Q. Xiong, B. Ding, J. Hou, D. Luo, Y. Rong, S. Li, State-of-health estimation and remaining useful life prediction for the lithium-ion battery based on a variant long short term memory neural network, *J. Power Sources.* 459 (2020), 228069, <https://doi.org/10.1016/j.jpowsour.2020.228069>.
- [28] C. Ma, X. Zhai, Z. Wang, M. Tian, Q. Yu, L. Liu, H. Liu, H. Wang, X. Yang, State of health prediction for lithium-ion batteries using multiple-view feature fusion and support vector regression ensemble, *Int. J. Mach. Learn. Cybern.* 10 (2019) 2269–2282, <https://doi.org/10.1007/s13042-018-0865-y>.
- [29] A. Adadi, M. Berrada, Peeking inside the black-box: A survey on explainable artificial intelligence (XAI), *IEEE Access.* 6 (2018) 52138–52160, <https://doi.org/10.1109/ACCESS.2018.2870052>.
- [30] N.V. Chawla, K.W. Bowyer, L.O. Hall, W.P. Kegelmeyer, SMOTE: Synthetic Minority Over-sampling Technique, *J. Artif. Intell. Res.* 16 (2002) 321–357, <https://doi.org/10.1613/jair.953>.
- [31] H. Han, W.Y. Wang, B.H. Mao, Borderline-SMOTE: a new over-sampling method in imbalanced data sets learning, *Int. Conf. Intell. Comput.* (2005) 878–887.
- [32] Z. Wang, T. Oates, Imaging time-series to improve classification and imputation, *IJCAI Int. Jt. Conf. Artif. Intell.* 2015-Janua (2015) 3939–3945.
- [33] D.F. Wang, Y. Guo, X. Wu, J. Na, G. Litak, Planetary gearbox fault classification by convolutional neural network and recurrence plot, *Appl. Sci.* 10 (2020) 1–11, <https://doi.org/10.3390/app10030932>.
- [34] J.-P. Eckmann, S.O. Kamphorst, D. Ruelle, Recurrence plots of dynamical systems, *Europhys. Lett.* 4 (1987) 973–977, <https://doi.org/10.1209/0295-5075/4/9-004>.
- [35] S. Khan, T. Yairi, A review on the application of deep learning in system health management, *Mech. Syst. Signal Process.* 107 (2018) 241–265, <https://doi.org/10.1016/j.ymssp.2017.11.024>.
- [36] B. Zhou, A. Khosla, A. Lapedriza, A. Oliva, A. Torralba, Learning deep features for discriminative localization, *Proc. IEEE Conf. Comput. Vis. Pattern Recognit.* (2016) 2921–2929, <https://doi.org/10.5465/ambpp.2004.13862426>.
- [37] Y. Bai, J. Yang, J. Wang, Y. Zhao, Q. Li, Image representation of vibration signals and its application in intelligent compound fault diagnosis in railway vehicle wheelset-axlebox assemblies, *Mech. Syst. Signal Process.* 152 (2021), 107421, <https://doi.org/10.1016/j.ymssp.2020.107421>.